International Journal of Engineering Trends and Technology
ISSN: 2231–5381 / https://doi.org/10.14445/22315381/IJETT-V71I9P217

Volume 71 Issue 9, 178-185, September 2023

Original Article

Frequency Characteristics of a Micro Electromechanical Gyroscope under Temperature Variations

Thuan-Hoang Tran[1], Quang-Vinh Nguyen[2], Van-Hao Lo[2], Tamara G. Nesterenko[2], Hanh C. Nguyen[3*]

[1]*Center of Electrical - Engineering, Duy Tan University, Danang, Vietnam.*
[2]*Academy of Military Sciences and Technologies, Hanoi, Vietnam.*
[3]*Faculty of Transportation Mechanical Engineering, The University of Danang- University of Science and Technology, Danang, Vietnam.*

[*]*Corresponding Author : nchanh@dut.udn.vn*

Received: 10 April 2023 Revised: 10 June 2023 Accepted: 17 August 2023 Published: 03 September 2023

Abstract *- The microelectromechanical (MEMS) gyroscope is designed as a vibrating gyroscope and consists of inertial masses supported by spring suspension over a glass substrate. The gyroscope has two channels of operation, which correspond to two modes: the driving mode and the sensitivity mode. The silicon-sensitive element of the MEMS gyroscope was designed to have natural frequencies of 12500 Hz for both the primary and secondary oscillations, with a frequency mismatch between them of no more than 10 Hz. This ensures that the gyroscope can accurately detect and measure rotational motion. To test the gyroscope, the sensitive element was packed in a case under a pressure of 10-2 Pa and subjected to varying temperatures to determine the temperature coefficients of change in the natural frequency of the primary and secondary oscillations. The temperature coefficients of change in the natural frequency of the primary and secondary oscillations were found to be 1.61 Hz/°C and 1.31 Hz/°C, respectively. This means that for every degree Celsius increase in temperature, the natural frequencies of the primary and secondary oscillations will change by those amounts. The testing results revealed that at a temperature of 20°C, the natural frequency of the primary oscillations was 12585 kHz, while the natural frequency of the secondary oscillations was 12609 kHz. These values are important for interpreting the output signals of the MEMS gyroscope and designing systems that use the gyroscope as a sensor.*

Keywords *- MEMS gyroscope, Natural frequency, Temperature coefficient, Rotational motion, Inertial masses.*

1. Introduction

The significance of microelectromechanical systems (MEMS) gyroscopes has been steadily growing. These devices are used in several fields like navigation, robotics[2], aerospace, and automotive engineering because of their small size, affordability, and precise performance [1]. Microelectromechanical systems (MEMS) gyroscopes function by harnessing the Coriolis effect, which arises when an item experiences rotational movement [3, 4]. The perpendicular deflection of the vibrating structure, induced by the Coriolis effect, is afterwards identified by the gyroscope as an output signal. The principal oscillation channel of the gyroscope is triggered by harmonic oscillations of inertial masses in accordance with the principle of operation. The gyroscope undergoes secondary oscillations of the inertial masses due to the Coriolis forces induced by angular velocities. Figure 1 illustrates the silicon sensor element of the gyroscope, including two constituent parts.

The technique of resonant excitation is often used to induce primary oscillations [5-7]. By exciting the vibrational structure at its inherent frequency and with a high-quality factor, this approach facilitates the amplification of oscillations. In order to further improve the quality factor, the vibrational structure is encased inside a hermetically sealed casing to maintain a vacuum environment [9]. This configuration is used to optimize oscillation amplitudes across diverse applications. Nevertheless, the silicon structure exhibits susceptibility to variations in the surrounding temperature, resulting in thermal strain inside the structure.

This, in turn, modifies the stiffness coefficient of the suspension beams and thus affects the intrinsic frequencies of both the primary and secondary oscillations. Moreover, the performance of the gyroscope is influenced by the temperature-dependent viscosity of the gaseous medium present inside the casing. The sensitivity properties of the gyroscope may be significantly affected by temperature variations, leading to a temperature drift in the MEMS gyroscope's output signal excitation and processing system.

In order to examine the influence of temperature on the dynamic properties of the gyroscope, this research work examines the implementation of elastic suspensions in both the main and secondary oscillation channels.

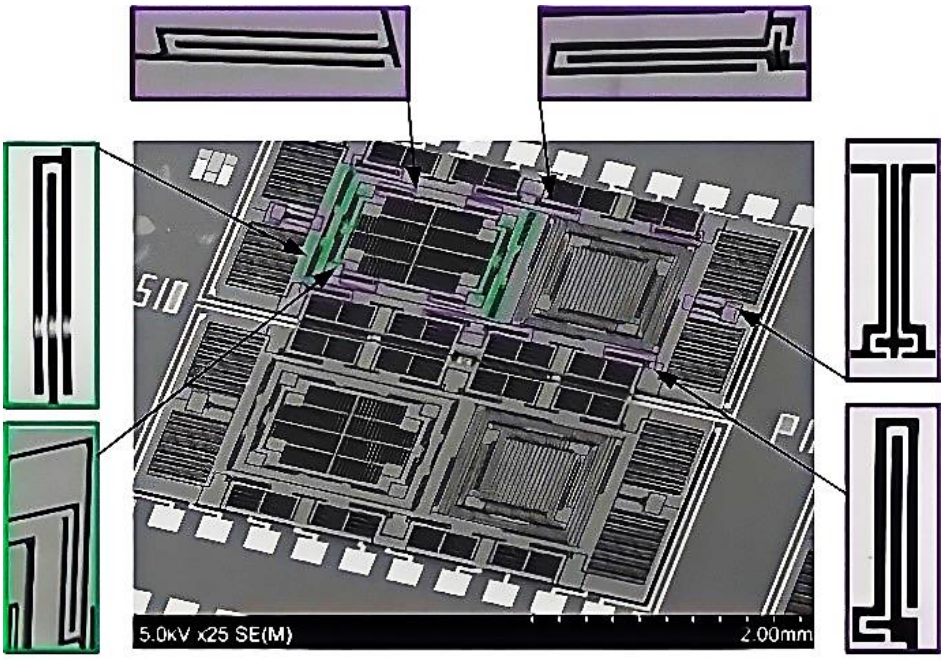

Fig. 1 Silicon design of the MEMS gyroscope

Additionally, a mathematical model is proposed to elucidate the impact of temperature on the natural frequencies. In addition, empirical findings are also provided as evidence to substantiate the mathematical framework.

2. Elastic Element Modeling in the Channel of Primary Oscillations

The primary oscillation channel in a symmetrical structure can be simplified as a system of inertial masses and elastic elements, as depicted in Figure 2.

The third type of elastic element (Figure 3) suspends the inertial mass above the glass substrate. All elastic elements have the same stiffness coefficients, where:

$$k_1 = k_2 = k_3 = k_4 = k_1 = k_2 = k_3 = k_4 = k_{y1}$$
$$k_5 = k_6 = k_7 = k_8 = k_5 = k_6 = k_7 = k_8 = k_{y2}$$
$$k_9 = k_{10} = k_9 = k_{10} = k_{y3}$$

The intrinsic frequency of main oscillations can be calculated using formula (1)

$$f_y = \frac{1}{2\pi} \cdot \sqrt{\frac{k_y}{m_y}} \quad (1)$$

where m_y is the mass of the moving body in the primary oscillation channel.

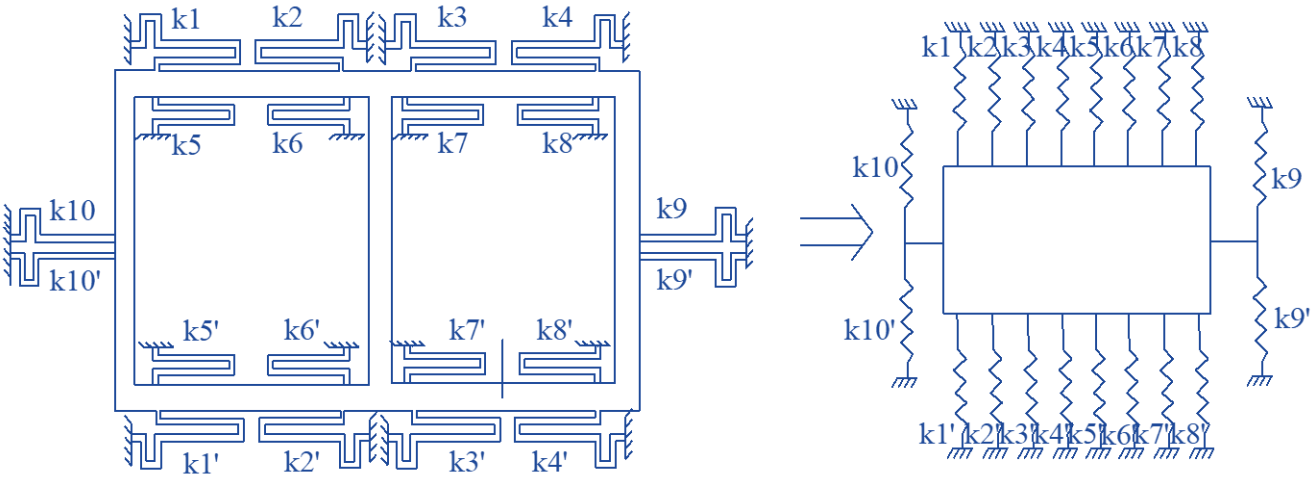

Fig. 2 Simplified primary channel system

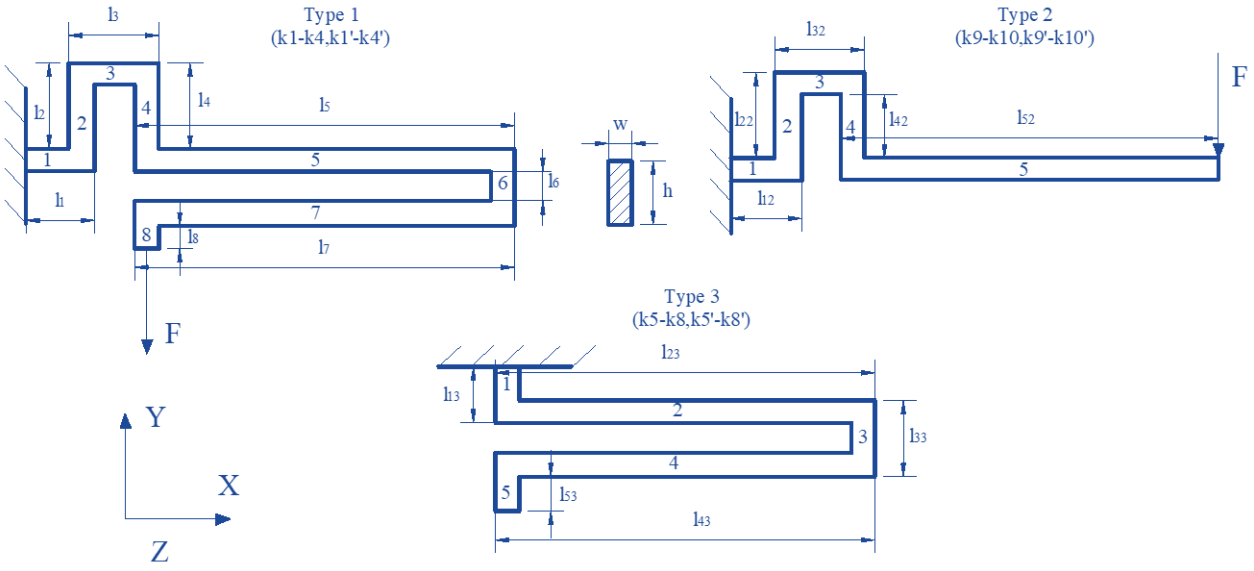

Fig. 3 Models of elastic elements in the channel of primary vibrations

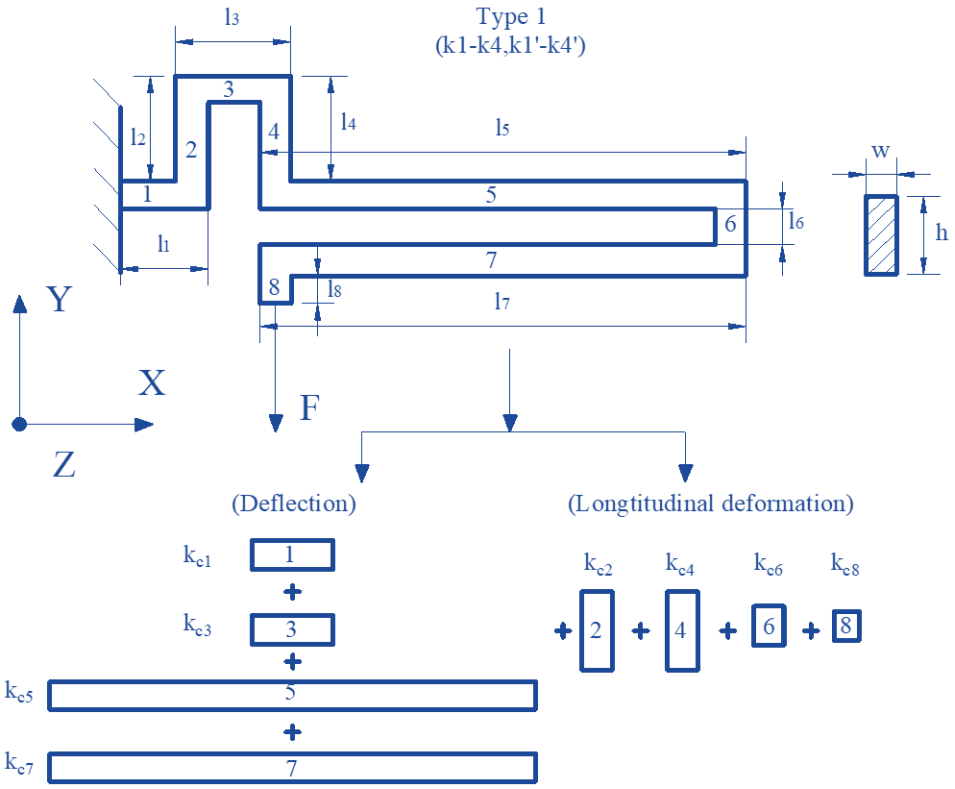

Fig. 4 Design of the first type of elastic elements

The design of the first type of elastic element is shown in Figure 4. This elastic element can be divided into separate sections with two types of deformation when analyzing and calculating stiffness under the influence of force F along the Y-axis, namely longitudinal deformation and deflection [10-12]. Where m_y - is the mass of the moving body; k_1, k_2, k_3, k_4, k_5, k_6, k_1', k_2', k_3', k_4', k_5' and k_6' are stiffness coefficients of elastic elements of the first type; h– height, and w– width of the elastic elements; l_1, l_2, l_3, l_4, l_5, l_6, l_7, l_8 are the lengths of the elastic elements of the first type; l_{12}, l_{22}, l_{32}, l_{42}, l_{52} are the lengths of elastic elements of the second type; l_{13}, l_{23}, l_{33}, l_{43}, l_{53} are the lengths of elastic elements of the third type. The first type of elastic element's stiffness coefficient, consisting of eight components connected in series, can be determined by equation (2):

$$\frac{1}{k_{y1}} = \frac{1}{k_{c1}} + \frac{1}{k_{c3}} + \frac{1}{k_{c5}} + \frac{1}{k_{c7}} + \frac{1}{k_{c2}} + \frac{1}{k_{c4}} + \frac{1}{k_{c6}} + \frac{1}{k_{c8}} \quad (2)$$

Assuming the mass of the moving body is much greater than that of the elastic element, which can be neglected, the stiffness coefficient of the first type of elastic element, k_y, can be determined by checking the deformations of all sections caused by the force F acting on its free end. The elastic element in Figure 3 is fixed at one end and loaded with a force F along the Y direction at the other end. According to [10], the deformation of the beam can be determined using equation (3):

$$\varepsilon(y) = \int \frac{N(y)}{E \cdot w \cdot h} \cdot \frac{\partial N(y)}{\partial F} \cdot dy + \int \frac{M(x)}{E \cdot I_z} \cdot \frac{\partial M(x)}{\partial F} \cdot dx \quad (3)$$

Longitudinal deformation of the elastic element occurs in sections (2, 4, 6, 8) under the influence of force *F*. The axial tensile force N_2 and longitudinal deformation ε_2 of section 2 with length l_2 can be determined using equation (4), while the axial compressive force N_4 and longitudinal deformation ε_4 of section 4 with length l_4 can be expressed using equation (5).

$$\begin{cases} N_2(y) = F(y), 0 \le y \le l_2 \\ \varepsilon_2 = \int \frac{F(y)}{E \cdot w \cdot h} \cdot \frac{\partial F(y)}{\partial F} \cdot dy = \frac{F \cdot l_2}{E \cdot w \cdot h} \end{cases} \quad (4)$$

$$\begin{cases} N_4(y) = F(y), 0 \le y \le l_4 \\ \varepsilon_4 = \int \frac{F(y)}{E \cdot w \cdot h} \cdot \frac{\partial F(y)}{\partial F} \cdot dy = \frac{F \cdot l_4}{E \cdot w \cdot h} \end{cases} \quad (5)$$

Similarly, axial forces and longitudinal deformations of sections 6 and 8 can be determined using similar formulas.

$$\begin{cases} N_6(y) = F(y), 0 \le y \le l_6 \\ \varepsilon_6 = \frac{F \cdot l_6}{E \cdot w \cdot h} \end{cases}$$

and

$$\begin{cases} N_8(y) = F(y), 0 \le y \le l_8 \\ \varepsilon_8 = \frac{F \cdot l_8}{E \cdot w \cdot h} \end{cases} \quad (6)$$

Sections 1, 3, 5, and 7 bend in the Y direction under the action of force F. The deflections of the sections have the following form:

$$\begin{cases} \varepsilon_1 = \int_0^{l_1} \frac{F \cdot x}{E \cdot I_z} \cdot \frac{\partial (F \cdot x)}{\partial F} \cdot dx = \frac{F \cdot {l_1}^3}{3 \cdot E \cdot I_z} \\ \varepsilon_3 = \int_0^{l_3} \frac{F \cdot x}{E \cdot I_z} \cdot \frac{\partial (F \cdot x)}{\partial F} \cdot dx = \frac{F \cdot {l_3}^3}{3 \cdot E \cdot I_z} \end{cases}$$

and

$$\begin{cases} \varepsilon_5 = \int_0^{l_5} \frac{F \cdot x}{E \cdot I_z} \cdot \frac{\partial (F \cdot x)}{\partial F} \cdot dx = \frac{F \cdot {l_5}^3}{3 \cdot E \cdot I_z} \\ \varepsilon_7 = \int_0^{l_7} \frac{F \cdot x}{E \cdot I_z} \cdot \frac{\partial (F \cdot x)}{\partial F} \cdot dx = \frac{F \cdot {l_7}^3}{3 \cdot E \cdot I_z} \end{cases} \quad (7)$$

According to Hooke's law, the stiffness coefficient of the first type of elastic element is defined as [7]:

$$k_{y1} = \frac{3 \cdot E \cdot w \cdot h \cdot I_z}{3 \cdot I_z \cdot (l_2 + l_4 + l_6 + l_8) + w \cdot h \cdot ({l_1}^3 + {l_3}^3 + {l_5}^3 + {l_7}^3)} \quad (8)$$

Similarly, the stiffness coefficients of elastic elements of the second and third types are calculated using formulas (9) and (10):

$$k_{y2} = \frac{3 \cdot E \cdot w \cdot h \cdot I_z}{3 \cdot I_z \cdot (l_{22} + l_{42}) + w \cdot h \cdot ({l_{12}}^3 + {l_{32}}^3 + {l_{52}}^3)} \quad (9)$$

$$k_{y3} = \frac{3 \cdot E \cdot w \cdot h \cdot I_z}{3 \cdot I_z \cdot (l_{13} + l_{33} + l_{53}) + w \cdot h \cdot ({l_{23}}^3 + {l_{43}}^3)} \quad (10)$$

2.1. Models of Elastic Elements in Secondary Oscillation Channels

In the channel of secondary oscillations, the MEMS gyroscope exhibits sensitivity along two axes, the X and Z axes [13-15]. However, this study will concentrate on the design of secondary oscillations in the X direction, as shown in Figure 1. To suspend the inertial mass above the substrate in the channel of secondary vibrations, two types of elastic elements are used (as shown in Figure 5). The stiffness coefficients of these elastic elements are calculated in a similar manner to that of the primary vibration channel.

$$k_{x1} = \frac{3 \cdot E \cdot w \cdot h \cdot I_z}{3 \cdot I_z \cdot (l_{14} + l_{34} + l_{54}) + w \cdot h \cdot ({l_{24}}^3 + {l_{44}}^3)} \quad (11)$$

$$k_{x2} = \frac{3 \cdot E \cdot w \cdot h \cdot I_z}{3 \cdot I_z \cdot (l_{15} + l_{35}) + w \cdot h \cdot ({l_{25}}^3 + {l_{45}}^3)} \quad (12)$$

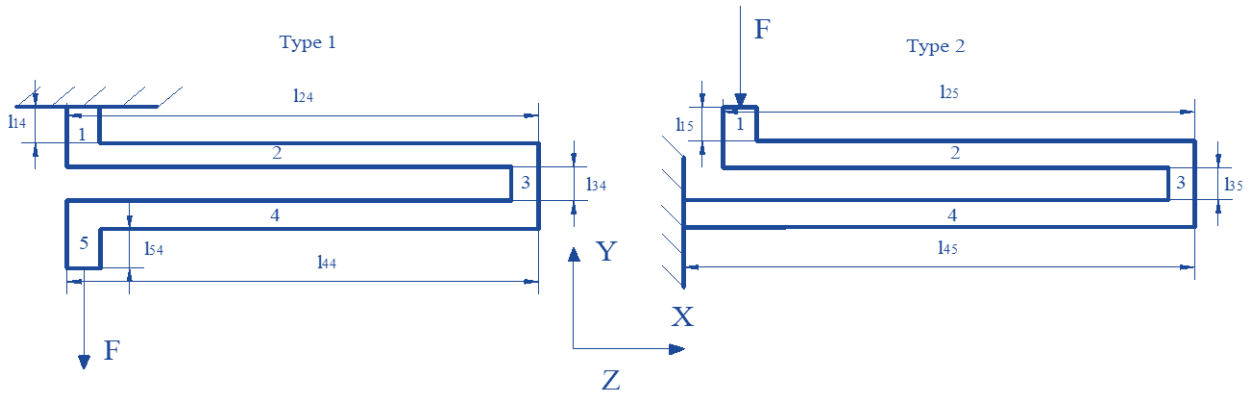

Fig. 5 The elastic element models for the X-directional sensitivity channel in secondary oscillations

The natural frequency of secondary oscillations along the X-axis is given by equation (13):

$$f_x = \frac{1}{\pi} \cdot \sqrt{\frac{k_{x1}+k_{x2}}{m_x}} \quad (13)$$

Here, m_x represents the mass of the movable body in the channel of secondary oscillations along the X-axis and k_{x1} and k_{x2} represent the stiffness of the two different types of elastic elements used in the suspension system. It should be noted that Young's modulus is temperature-dependent [16-18]. The equation for calculating Young's modulus at temperature is given by equation (14):

$$E(T_1) = E(T_0) \cdot [1 - 5 \cdot 10^{-5} \cdot (T_1 - T_0)] \quad (14)$$

Figure 6 illustrates the dependence of natural frequencies on temperature within the range of -20ºC to 80ºC, using the mathematical models and parameters of elastic elements provided in Tables 1-2. The graph shows that the natural frequency of primary oscillations decreases with increasing ambient temperature, with an average frequency change factor of 0.31 Hz/°C within the given temperature range.

Table 1. Elastic elements parameters in the channel of primary vibrations

Parameters	Value (µm)	Parameters	Value (µm)
l_1	10	l_{52}	190
l_2	15	l_{13}	10
l_3	15	l_{23}	250
l_4	15	l_{12}	10
l_5	230	l_{22}	10
l_6	10	l_{32}	10
l_7	220	l_{33}	10
l_8	10	l_{42}	10
w	6	l_{43}	250
h	40	l_{53}	10

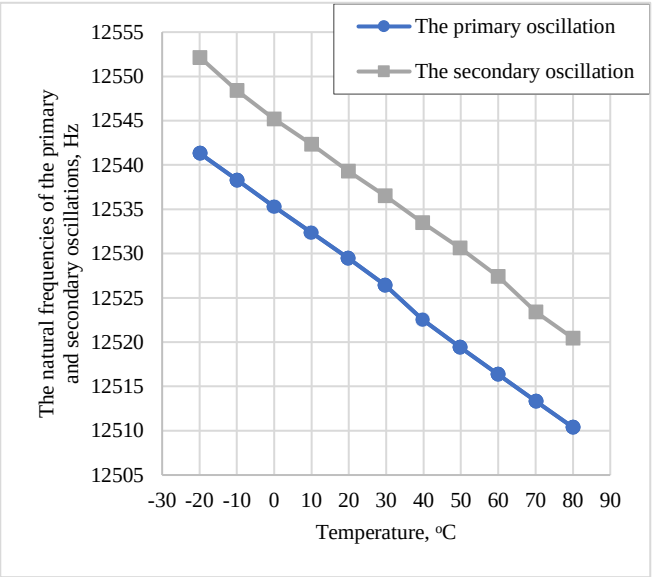

Fig. 6 Dependence of natural frequencies on temperature

Table 2. Parameters of first-type and second-type elastic elements

Section	Type 1 (µm)	Type 2 (µm)
1	10	10
2	225	180
4	10	10
4	225	190
5	10	-
6	-	-

Similarly, the natural frequency of secondary oscillations also decreases with an increase in ambient temperature, with an average frequency change factor of 0.32 Hz/°C in the secondary oscillation channel.

2.2. Elastic Element Models in the Channel of Secondary Oscillations

At the design and simulation stage, only the impact of temperature on the silicon structure of the MEMS gyroscope is considered, without taking into account the base material [19]. The simulation results show that the natural frequencies of both primary and secondary oscillations decrease as the temperature increases.

However, practical studies have shown that the natural frequencies increase with temperature. This positive frequency change is due to the significant axial stress caused by the mismatch between the thermal linear expansion coefficients of the silicon structure and the glass substrate, as noted in references [16] and [20].

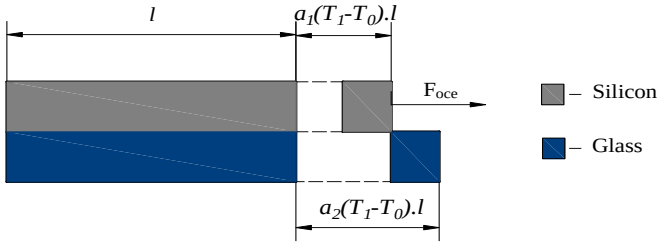

Fig. 7 Effect of temperature change on axial reinforcement between bonded materials

The MEMS gyroscope is manufactured using the "silicon on glass" technology, where the inertial masses are fixed above the substrate on clamping glass anchors through elastic elements. The influence of temperature on the structure of the MEMS gyroscope primarily arises from the disparity between the silicon structure's thermal linear expansion coefficients (TLECs) and the glass substrate.

This leads to a mechanical axial stress along with the elastic elements, causing a shift in the natural frequency [20]. The connection of a silicon structure with a glass substrate on anchors can be considered as two plates attached with the same length *l*, but different TLECs $\alpha 1$ and $\alpha 2$ (as shown in Figure 7). The temperature dependences of the TLECs of silicon and glass can be expressed by the following formulas (15-17):

$$\alpha_1 = 2{,}3616 \cdot 10^{-6} + 1{,}0323 \cdot 10^{-8} \cdot \mathrm{T}_1 - 3{,}2251 \cdot 10^{-11} \cdot \mathrm{T}_1^2 + 4{,}8818 \cdot 10^{-14} \cdot \mathrm{T}_1^3 \quad (15)$$

$$\alpha_2 = 3{,}2847 \cdot 10^{-6} + 1{,}5247 \cdot 10^{-9} \cdot \mathrm{T}_1 - 1{,}053 \cdot 10^{-11} \cdot \mathrm{T}_1^2 + 1{,}389 \cdot 10^{-14} \cdot \mathrm{T}_1^3 \quad (16)$$

$$\sigma_{\mathrm{oce}} = w \cdot h \cdot E(T_1) \cdot (\alpha_2 - \alpha_1) \cdot (T_1 - T_0) \cdot (1 - \nu_{si}) \quad (17)$$

Figure 8 illustrates the temperature-dependent variations of LTEC for two materials, namely, silicon and the glass utilized. Within the temperature range of up to 140ºC, the CLTE of glass exceeds that of silicon, implying that the glass anchor expands at a faster rate than silicon elastic components upon an increase in temperature. As a result, the elastic elements experience axial stress. The axial stress resulting from a temperature variation from T_0 to T_1 can be computed as indicated in previous studies [20], [23, 24]. The formula characterizing the ratio between the natural frequencies of primary and secondary oscillations and the axial stress:

$$f_y(T_1) = \frac{1}{2\pi}\sqrt{\begin{matrix}\frac{k_{y1}}{m_y}\cdot\left(1+\frac{\sigma_{\mathrm{oce}}(T_1)\cdot(l_1+l_3+l_5+l_7)^2}{3{,}5\cdot E(T_1)\cdot w^2}\right)\\ +\frac{k_{y2}}{m_y}\cdot\left(1+\frac{\sigma_{\mathrm{oce}}(T_1)\cdot(l_{12}+l_{32}+l_{52})^2}{3{,}5\cdot E(T_1)\cdot w^2}\right)\\ +\frac{k_{y3}}{m_y}\cdot\left(1+\frac{\sigma_{\mathrm{oce}}(T_1)\cdot(l_{23}+l_{43})^2}{3{,}5\cdot E(T_1)\cdot w^2}\right)\end{matrix}} \quad (18)$$

$$f_x(T_1) = \frac{1}{2\pi}\sqrt{\frac{k_{x1}}{m_x}+\frac{k_{x2}}{m_x}\cdot\left(1+\frac{\sigma_{\mathrm{oce}}(T_1)\cdot(l_{25}+l_{45})^2}{3{,}5\cdot E(T_1)\cdot w^2}\right)} \quad (19)$$

Figure 9 illustrates the dependence of the inherent frequencies on temperature, considering thermal axial stress. These graphs were obtained by using the modeling formulas (16) with the parameters provided in Tables 1 and 2. It is observed that in the temperature range below 140ºC, the LTEC of glass is higher than that of silicon, leading to thermal axial stress due to the mismatch in CLTEs. However, as the temperature rises to 140ºC, the TCLEs of silicon and glass converge, resulting in a decrease in the magnitude of the thermal axial stress.

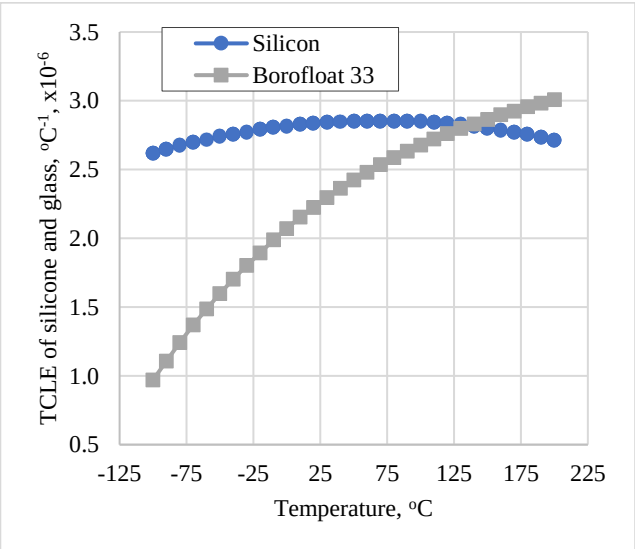

Fig. 8 Temperature dependences of LTEC of silicon and glass

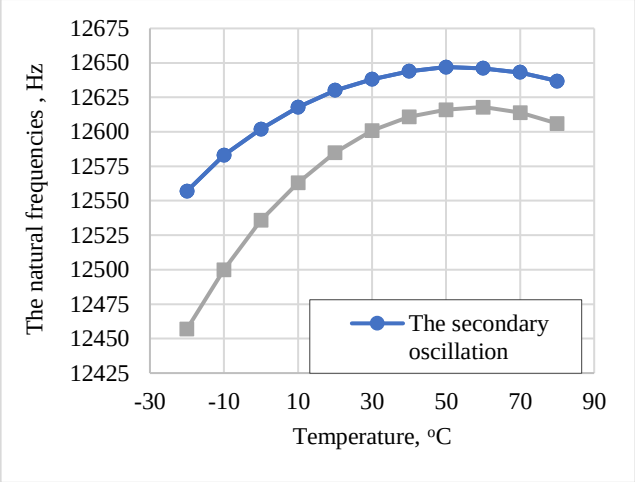

Fig. 9 Impact of temperature on the inherent frequencies

The graphs in Figure 9 indicate that the increase in inherent frequencies is not equal. The natural frequency changes of primary oscillations in the temperature range from -20°C to 80°C is 1.57 Hz/°C, which is higher than the natural frequency changes of secondary oscillations, which are equal to 0.83 Hz/°C. Moreover, the temperature change affects the natural frequency matching between primary and secondary oscillations, resulting in a decrease in the scale factor, stability, and accuracy of the measurement.

2.3. Experimental Setup and Test Results

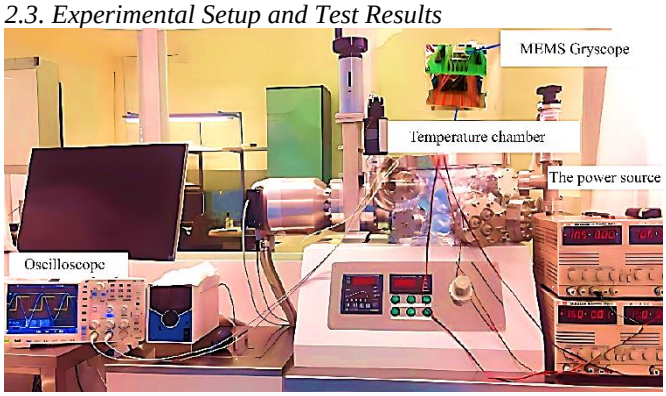

Fig. 10 Experimental setup

This study focused on analyzing a gyroscope produced by micro-electromechanical systems (MEMS) to investigate the impact of thermal axial stress on the natural frequencies. To conduct this investigation, temperature tests were performed within a controlled environment using a specialized temperature chamber. The power source, control signal, and output signal were connected directly to the thermal chamber (as illustrated in Figure 10) to ensure accurate and reliable results.

The temperature testing process consisted of gradually increasing the temperature from -20°C to 80°C, with increments of 10°C at a time. At each temperature level, the conditions were kept constant for 10 minutes to allow for proper measurements. The amplitude-frequency characteristics of the two channels were measured using an oscilloscope, and the results were recorded for analysis. The test results are presented in Figures 11 and 12.

Figure 11 displays the natural frequency dependence of primary and secondary oscillations on temperature. The experimental data shows that resonant oscillations were observed at a frequency of about 12.55 kHz. As the temperature increased from -20ºC to 80ºC, the natural frequency of primary oscillations increased from 12.499 kHz to 12.660 kHz. Conversely, the resonant amplitude of the excited oscillations decreased with increasing temperature. The observed decrease in the amplitude of oscillations with increasing temperature can be attributed to the decrease in the quality factor of the gyroscope. The natural frequency and amplitude of the oscillations exhibited an average temperature coefficient of change of 1.61 Hz/°C and 8.5 mV/°C, respectively. The natural frequency dependence of primary oscillations on temperature is displayed in Figure 11. It is important to highlight that the inherent frequency of secondary oscillations is greater than that of primary oscillations. The frequency mismatch takes on a value of Hz at a temperature of 20ºC, and this mismatch decreases with increasing temperature. The average temperature coefficient of change was 1.31 Hz/°C.

Figure 12 shows the amplitude variation of primary oscillations with temperature and its correlation with natural frequency dependence. This decrease in quality factor affects the ability of the gyroscope to maintain its resonant frequency in response to changing temperature.

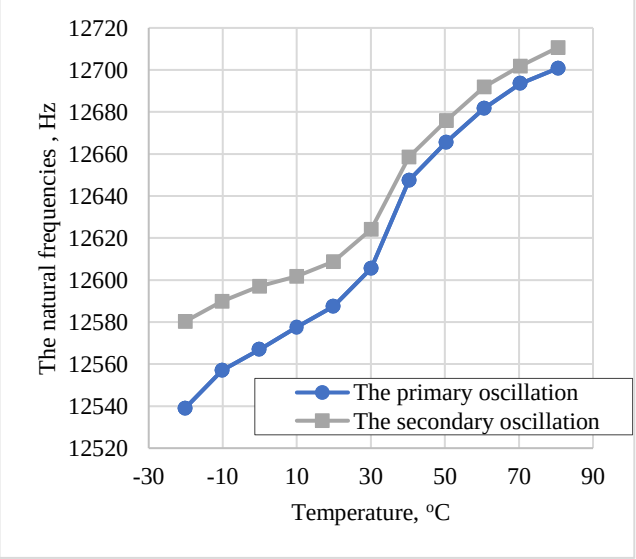

Fig. 11 Primary oscillations natural frequency variation with temperature

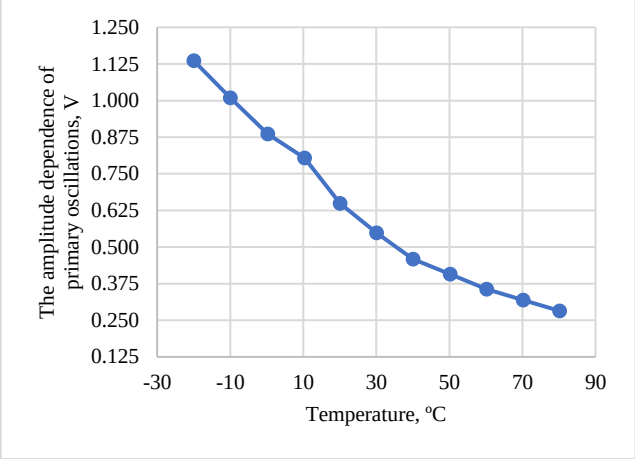

Fig. 12 The amplitude variation of primary oscillations with temperature and its correlation with natural frequency dependence

The average temperature coefficients of change in natural frequency and amplitude were found to be 1.61 Hz/°C and 8.5 mV/°C, respectively. In Figure 11, we observe an increase in natural frequency in the channel of secondary oscillations. This increase indicates that the secondary oscillations have a higher natural frequency than the primary oscillations.

3. Conclusion

To obtain accurate and reliable results from a MEMS gyroscope, the effects of axial stress should be taken into account. The study revealed that temperature exerts a significant influence on the inherent frequencies of both primary and secondary vibrations, with a negative change observed when axial stress is not taken into account. However, when the effects of axial stress are considered, a positive change in the natural frequencies is observed. This highlights the importance of accounting for axial stress in the design and operation of MEMS gyroscopes, as it can greatly impact their performance and accuracy. The experimental results present significant insights into the impact of thermal axial stress on the inherent frequencies of primary and secondary oscillations in a MEMS gyroscope. The study indicates that the natural frequency of primary oscillations rises with an increase in temperature while the amplitude of the excited oscillations diminishes. Furthermore, the inherent frequency of secondary oscillations is higher than that of primary oscillations, and the frequency mismatch between them decreases as the temperature increases. The average temperature coefficients of change in natural frequency and amplitude were also determined to be 1.61 Hz/°C and 8.5 mV/°C, respectively, for the gyroscope. These findings are significant in understanding the behavior of MEMS gyroscopes under thermal stress, which can inform future design and optimization of such devices.

Acknowledgments

This research is financially supported by The University of Danang, University of Science and Technology, under project number T2021-02-33.

References

[1] V. Raspopov, *Micromechanical Devices: Studies, Allowance*, Moscow, *Mechanical Engineering*, pp. 83–91, 2007.

[2] Ngan T.T. Le, and Huyen T.T. Tran, "Robot Control Based on Image Processing to Follow the Target," *SSRG International Journal of Electrical and Electronics Engineering*, vol. 7, no. 4, pp. 5-8, 2020. [CrossRef] [Publisher Link]

[3] State-of-the-art MEMS Gyroscopes and Accelerometers. [Online]. Available: https://sovtest-ate.com/news/publications/sovremennye-mems_giroskopy-i-akselerometry/

[4] C.V.Roja et al., "Intelligent Safety using Smart Blackbox," *SSRG International Journal of Electronics and Communication Engineering*, vol. 5, no. 3, pp. 5-9, 2018. [CrossRef] [Publisher Link]

[5] Cenk Acar, and Andrei Shkel, *MEMS Vibratory Gyroscopes: Structural Approaches to Improve Robustness* MEMS, Reference Shelf: Springer Publishing Company, Incorporated, 2008. [Google Scholar] [Publisher Link]

[6] Korhan Sahin et al., "A Wide-Bandwidth and High-Sensitivity Robust Microgyroscope," *Journal of Micromechanics and Micro Engineering*, vol. 19, no. 7, 2009. [CrossRef] [Google Scholar] [Publisher Link]

[7] Lili Dongand David Avanesian, "Drive-Mode Control for Vibrational MEMS Gyroscopes," *IEEE Transactions on Industrial Electronics*, vol. 56, no. 4, pp. 956-963, 2009. [CrossRef] [Google Scholar] [Publisher Link]

[8] K. Tejaswini, and S. Sreenivasa Rao, "Quick Response System for Road Accidents with Automatic Accident Detection and Prevention Using IoT," *International Journal of Computer Trends and Technology*, vol. 71, no. 1, pp. 8-16, 2023. [CrossRef] [Publisher Link]

[9] C. T. C. Nguyen, "Micromechanical Resonators for Oscillators and Filters," *1995 IEEE Ultrasonics Symposium, Proceedings of an International Symposium*, vol. 1, pp. 489-499, 1995. [CrossRef] [Google Scholar] [Publisher Link]

[10] S. Timoshenko, *Vibration Problems in Engineering*, The Journal of the Royal Aeronautical Society, vol. 59, pp. 781-781, 2016.

[11] R. V. Southwell, *An Introduction to the Theory of Elasticity for Engineers and Physicists*, Cambridge University Press, 2016.

[12] S. Graham Kelly, *Mechanical Vibrations: Theory and Applications*, SL ed., Cengage Learning, 2011. [Publisher Link]

[13] Zhiwei Kouet al., "Investigation, Modeling, and Experiment of an MEMS S-Springs Vibrating Ring Gyroscope," *Journal of Micro/Nanolithography, MEMS, and MOEMS*, vol. 17, no. 1, 2018. [CrossRef] [Google Scholar] [Publisher Link]

[14] Pavel Baranovet al., "A Novel Multiple-Axis MEMS Gyroscope-Accelerometer with Decoupling Frames," *Sensor Review*, vol. 39, no. 5, pp. 670-681, 2019. [CrossRef] [Google Scholar] [Publisher Link]

[15] Ramya Ravibarathi, and Tamilarasu Viswanathan, "Assimilation of Gesture using 9 Axis Acclerometer Sensor," *SSRG International Journal of Electrical and Electronics Engineering*, vol. 5, no. 2, pp. 1-4, 2018. [CrossRef] [Google Scholar] [Publisher Link]

[16] Zhanqiang Hou et al., "Effect of Axial Force on the Performance of Micromachined Vibratory Rate Gyroscopes," *Sensors*, vol. 11, no. 1, pp. 296-309, 2011. [CrossRef] [Google Scholar] [Publisher Link]

[17] Dunzhu Xia et al., "MicrogyroscopeTemperature Effects and Compensation-Control Methods," *Sensors*, vol. 9, no. 10, pp. 8349-8376, 2009. [CrossRef] [Google Scholar] [Publisher Link]

[18] Mohamed Ali Belaid, "Temperature Effects in a Power RF LDMOS Device Performance Due to Hot Carrier," *SSRG International Journal of Electrical and Electronics Engineering*, vol. 9, no. 4, pp. 1-6, 2022. [CrossRef] [Publisher Link]

[19] Pham Anh Tuan et al., "Micro-Opto-Electro-Mechanical Transducers for Measurement and Control Systems," *SSRG International Journal of Electrical and Electronics Engineering*, vol. 5, no. 10, pp. 7-11, 2018. [CrossRef] [Publisher Link]

[20] A. Bokaian, "Natural Frequencies of Beams Under Tensile Axial Loads," *Journal of Sound and Vibration*, vol. 142, no. 8, pp. 481-498, 1990. [CrossRef] [Google Scholar] [Publisher Link]

[21] Matthew A. Hopcroft, William D. Nix, and Thomas W. Kenny, "What is the Young's Modulus of Silicon?," *Journal of Micro Electro Mechanical Systems*, vol. 19, pp. 229-238, 2010. [CrossRef] [Google Scholar] [Publisher Link]

[22] Chu-Hyung Cho, Ho-Young Cha, and Hyuk-Kee Sung, "Characterization of Stiffness Coefficients of Silicon Versus Temperature Using "Poisson's Ratio" Measurements," *JSTS: Journal of Semiconductor Technology and Science*, vol. 16, no. 2, pp. 153-158, 2016. [Google Scholar] [Publisher Link]

[23] Leonid S. Sinev, "Mechanical Stresses Estimation in Silicon and Glass Bonded at Elevated Temperature," *Science and Education of the Bauman MSTU*, no. 12, pp. 951-965, 2014. [CrossRef] [Google Scholar] [Publisher Link]

[24] Bongsang Kim et al., "Temperature Dependence of Quality Factor in MEMS Resonators," *Journal of Micro Electro Mechanical Systems*, vol. 17, no. 3, pp. 755-766, 2008. [CrossRef] [Google Scholar] [Publisher Link]